Chapter 7

Near-Axial Flow

The preceding chapters (3–6) deal with simulations of turbulent boundary layers on cylinders in axial flow. Attention is given here to flows with the free-stream inclined at an angle β to the cylinder axis, as defined in figure 2.1. The numerical scheme used for the yawed-flow simulations is that described in chapter 2, for which the axial-flow simulations are simply the special case $\beta = 0$.

Attention is first given to simulations of turbulent boundary layers in a range of yawed-flow conditions. The effects of yaw on flow statistics and instantaneous turbulence structures are investigated. The second section considers flow at a yaw angle that is large enough to produce a form of vortex-shedding. The frequency of vortex-shedding is compared with available experiments, and instantaneous flow structures are examined. The main findings are summarised at the end of the chapter.

7.1 Turbulent Near-Axial Flow

7.1.1 Computational Considerations

The simulation procedure described in chapter 2 is designed for both axial flow and yawed flow over cylinders. However, the collection of flow statistics is more difficult for yawed flow than it is for axial flow. This is because statistics for axial flow are axisymmetric, whereas those for yawed flow vary from the windward to the leeward side of the cylinder. The lack of axisymmetry in yawed flow implies that the outer radial boundary of the cylindrical computational domain may cause truncation and distortion of the flow on the leeward side of the cylinder in simulations of yawed flow produced by the present procedure.

To avoid possible distortion of the flow by the domain boundary, data produced for turbulent near-axial flow by the present simulation procedure are collected by use of the following method. Initial conditions for a simulation are taken from an axial-flow simulation at the statistically-steady state. The initial vorticity field is mapped onto a larger domain, and the simulation is advanced with the free-stream yaw angle set to the desired value. Data are recorded at intervals during the simulation, after a suitable development time but before significant vorticity accumulates near the outer domain boundary. The simulations are stopped well before the statistically-steady state is reached.

In principle, statistics can be ensemble-averaged across data sets generated from several initial states taken from the same axial-flow simulation, although this has not been feasible for the present study. Instead, averaging is performed over time and space. Temporal development of the flow implies that temporal averaging is only meaningful over short time intervals. The quantities presented here are temporally averaged using data from three time-steps over the interval $L_T = 50a/V_\infty$. Axial development of the flow is prevented by the periodic boundary conditions, therefore all quantities are averaged in the axial direction. In addition to temporal and axial averaging, the statistics are also averaged in the azimuthal direction. Statistics denoted with an overbar, for example $\overline{u_\tau}$, are averaged over the full azimuthal range ($\theta = 0$–2π radians). Where it is necessary to preserve the azimuthal distribution of a quantity, appropriate symmetry conditions are imposed about the X-axis and data are averaged over azimuthal sectors of width $\pi/8$ radians on each side of any given point. The resulting statistics are denoted with an underbar, for example $\underline{U_z}$.

The yawed-flow cases considered here are summarised on the left-hand-side of table 7.1. Mesh geometry parameters for the yawed-flow simulations are the same as those reported in table 3.1 for axial-flow simulations with corresponding values of Re_a and b/a.

7.1.2 Mean Flow

Mean-flow parameters for simulations of turbulent near-axial flow are given in table 7.1. The flow statistics depend on the yaw angle β, the Reynolds number Re_a, the elapsed simulation time t, and the initial conditions at $t = 0$.

The displacement thickness is a robust basis for comparison of the flows, as it is determined by integration of the mean velocity over the entire boundary layer. The

Case	β	Re_a	b/a	tV_∞/a	$\overline{u_\tau}/V_\infty$	$\overline{\delta}/a$	δ^*/a	θ^*/a
A1	0.25°	311	21	0	0.0726	3.81	0.874	0.637
A3				180	0.0685	6.41	1.273	1.021
B1	0.25°	674	12	0	0.0638	3.65	0.699	0.544
B2				150	0.0622	5.64	0.999	0.834
B3				325	0.0606	7.12	1.277	1.101
C1	0.25°	674	12	0	0.0634	1.65	0.403	0.252
C2				275	0.0622	5.23	0.974	0.805
C3				475	0.0592	6.94	1.287	1.102
D1	0.5°	674	12	0	0.0634	1.65	0.403	0.252
D2				300	0.0601	5.60	0.984	0.806

Table 7.1: Mean velocity parameters for turbulent near-axial flow

definitions of displacement and momentum thickness for yawed flow are similar to equations 4.8 and 4.9, but without the assumption of axisymmetry:

$$(\delta^* + a)^2 - a^2 = \frac{1}{\pi} \int_a^{a+\delta} \int_0^{2\pi} \left(1 - \frac{U_z}{V_{\infty z}}\right) r \, d\theta \, dr, \tag{7.1}$$

$$(\theta^* + a)^2 - a^2 = \frac{1}{\pi} \int_a^{a+\delta} \int_0^{2\pi} \frac{U_z}{V_{\infty z}} \left(1 - \frac{U_z}{V_{\infty z}}\right) r \, d\theta \, dr. \tag{7.2}$$

Contours of the mean axial velocity field are shown in figure 7.1. Sub-figure 7.1a shows results for two simulations (cases B2 and C2) with the same values of β (0.25°) and Re_a (674). The initial conditions used for the two simulations are from different axial-flow simulations at the statistically-steady state. Both of the axial-flow simulations used $Re_a = 674$ but with different domain radii, $b/a = 6$ (case B1) and $b/a = 3$ (case C1). After different non-dimensional times, $tV_\infty/a = 150$ (case B2) and $tV_\infty/a = 275$ (case C2), the two yawed-flow simulations produce turbulent boundary layers with similar values of δ^*/a (~ 0.99). The contours for the two flows are in reasonable agreement, indicating that the mean flow characterised by the values of β, Re_a and δ^*/a is essentially independent of the initial conditions after sufficient development time.

Sub-figure 7.1b shows two flow cases (A3 and C3) with different values of Re_a $(311, 674)$, the same yaw angle ($\beta = 0.25°$) and similar δ^*/a (~ 1.28). As Re_a increases from 311 to 674, the width of the contours (in the Y-direction) increases so that the contours become more circular. This effect may be due to the increased turbulence intensity that accompanies an increase in Re_a (and hence $\overline{a^+}$), as shown earlier for axial flow in figure 4.7. It is reasonable to suppose that increased turbulence intensity would enhance turbulent mixing in the boundary layer, which may

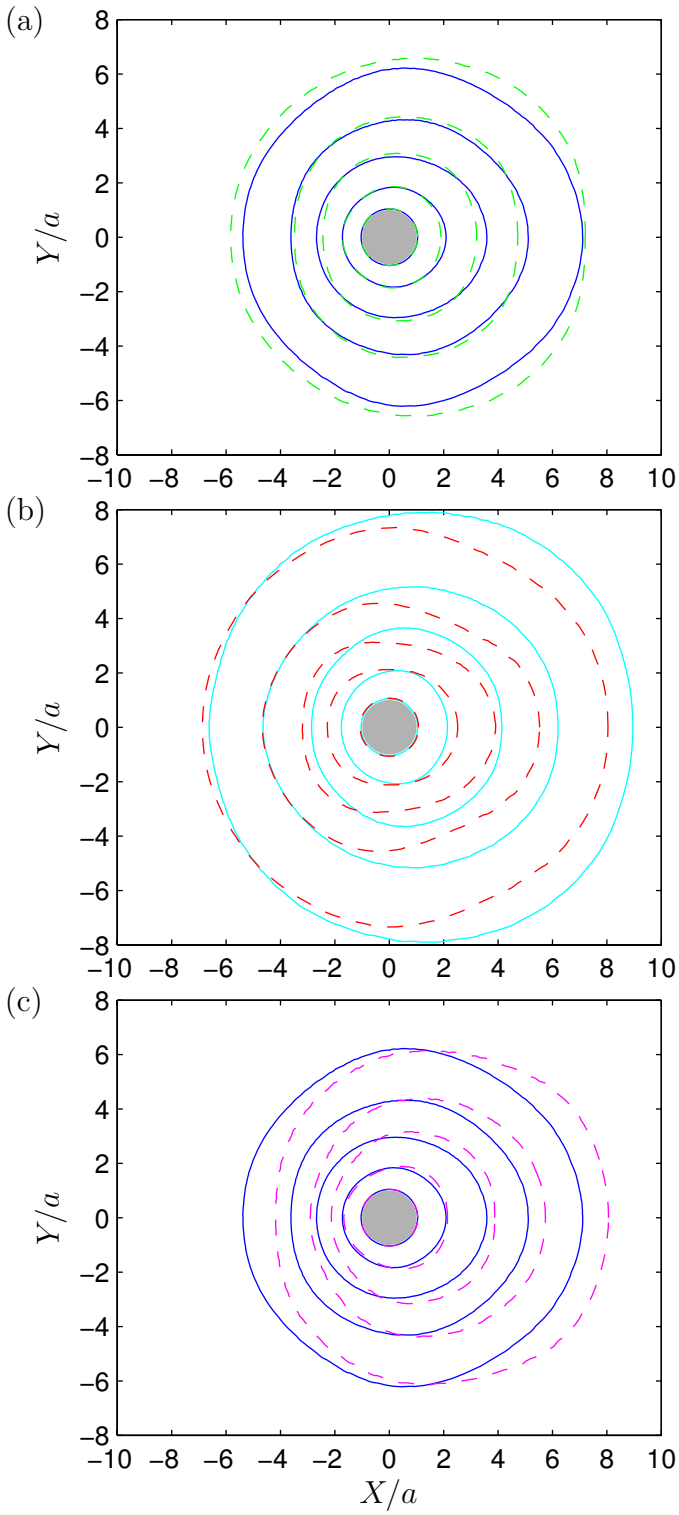

Figure 7.1: Contours of mean velocity for turbulent near-axial flow: $\underline{U_z}/V_{\infty z} = 0.1, 0.8, 0.9, 0.95, 0.99$. Varied parameters (see table 7.1): (a) initial conditions, – – B2 (from B1), —— C2 (from C1); (b) Reynolds number, – – A3 ($Re_a = 311$), —— C3 ($Re_a = 674$); (c) yaw angle, —— C2 ($\beta = 0.25°$), – – D2 ($\beta = 0.5°$).

tend to reduce the asymmetry of the boundary layer for a given free-stream yaw angle.

In sub-figure 7.1c, velocity contours are shown for cases C2 and D2, which have different yaw angles ($\beta = 0.25°, 0.5°$), the same Re_a (674) and similar δ^*/a (~ 0.98). As the yaw angle increases from 0.25° to 0.5°, contours move closer to the cylinder on the windward side and further away on the leeward side. The difference between the velocity contours of the two flows is much larger than may be expected intuitively for such a small difference in yaw angles (0.25°). However, the present results are consistent with the experimental results of Willmarth et al. [1977]. Their measurements for a yaw angle of $\beta = 1.06°$ (with $Re_a \approx 5000$) indicate that the boundary layer thickness on the leeward side of the cylinder is approximately ten times greater than the thickness on the windward side.

Comparison of flows with different values of δ^*/a is not undertaken here, because the present data do not span a wide range of δ^*/a values, excluding data taken from the initial development phase of the simulations. Such a comparison may be an interesting subject for future work.

The asymmetry of the mean velocity field in near-axial free-stream flow is evident in figure 7.2, which presents mean velocity profiles in wall units, based on the azimuthally averaged friction velocity $\overline{u_\tau}$, for flow cases C2 and D2 at several azimuthal positions around the cylinder. Outside the viscous sublayer, the velocity profiles are higher on the windward side ($\theta = \pi$) and lower on the leeward side ($\theta = 0$) of the cylinder. The difference between the windward and leeward profiles appears to increase as the yaw angle increases from 0.25° to 0.5° (with Re_a and δ^*/a held steady). In the logarithmic region, the yawed-flow profiles are shifted upwards or downwards depending on azimuthal position, but the slope of the profiles is nearly independent of azimuthal position and is very similar to that of the logarithmic region in axisymmetric flow with the same value of Re_a.

The above-mentioned effects of free-stream yaw on the logarithmic region are consistent with the experimental findings of Bücker and Lueptow [1998], indicating that the results of the present calculations are, at least, qualitatively correct. However, there are significant quantitative differences between the experimental data and the results of the present simulations. The discrepancy is probably due to the different values of the radius Reynolds number considered in the experiments ($Re_a \geq 2600$) and simulations ($Re_a = 674$)*.

*According to private communication with R. M. Lueptow, the values of the Reynolds number based on diameter reported by Bücker and Lueptow [1998] are too small by a factor of 4 due to an inadvertent calculation error.

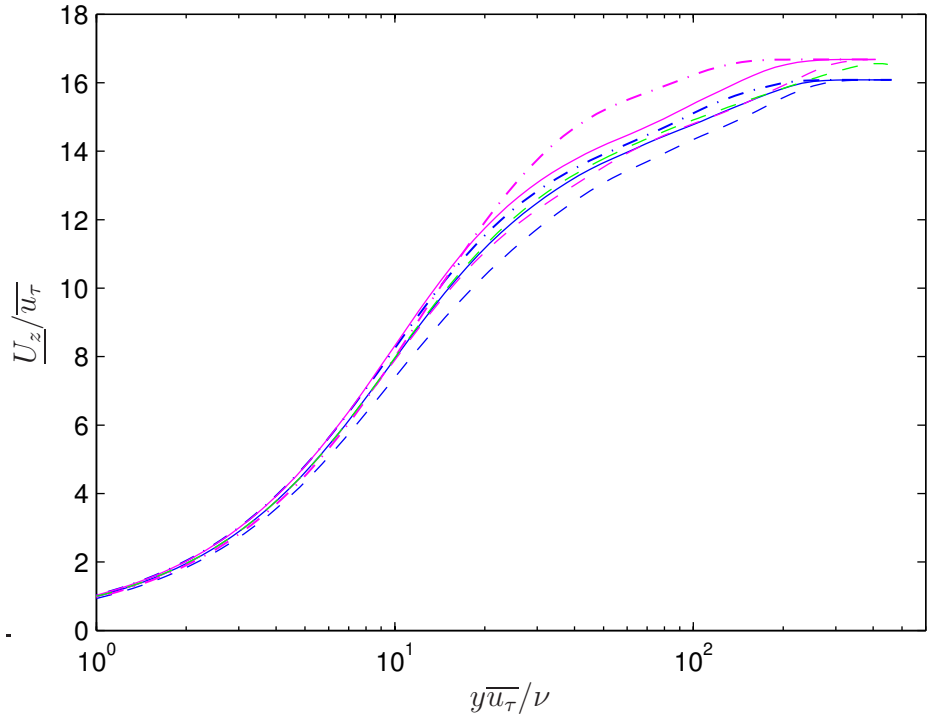

Figure 7.2: Mean velocity profiles in wall units for near-axial flow cases C2 and D2 ($Re_a = 674$, $\delta^*/a \approx 0.98$, $\beta = 0.25°$ and $0.5°$ respectively). Azimuthal positions ($\beta = 0.25°/\beta = 0.5°$): – – /– – $\theta = 0$, ——/—— $\theta = \pi/2$, · – · –/· – · – $\theta = \pi$. Axial flow: – – $Re_a = 674$, $b/a = 12$.

7.1.3 Turbulence Statistics

In this section, profiles of turbulence statistics for flow case D2 are examined. The flow has free-stream yaw angle $\beta = 0.5°$, Reynolds number $Re_a = 674$ and displacement thickness $\delta^*/a = 0.984$. Profiles are presented for the azimuthal positions $\theta = 0$ (leeward), $\theta = \pi$ (windward) and $\theta = \pi/2$. All profiles are non-dimensional with respect to azimuthally averaged values of either the friction velocity or the wall-shear-stress. The yawed-flow profiles are compared with those for axial flows at the same Reynolds number.

Reynolds shear-stresses are shown in figure 7.3. For the yawed-flow case, the Reynolds shear-stress as a function of $y\overline{u_\tau}/\nu$ is increased on the leeward side and decreased on the windward side of the cylinder, relative to the profile at $\theta = \pi/2$. Near the wall ($y\overline{u_\tau}/\nu \lesssim 100$), the profile at $\theta = \pi/2$ is similar to the axial-flow profiles.

The root-mean-square (RMS) fluctuations of each velocity component are shown in figure 7.4. As before, the yawed-flow profiles at $\theta = \pi/2$ are similar, near the wall ($y\overline{u_\tau}/\nu \lesssim 100$), to the axisymmetric profiles. Compared with the profiles for $\theta = \pi/2$, the yawed-flow profiles are higher on the leeward side and lower on the

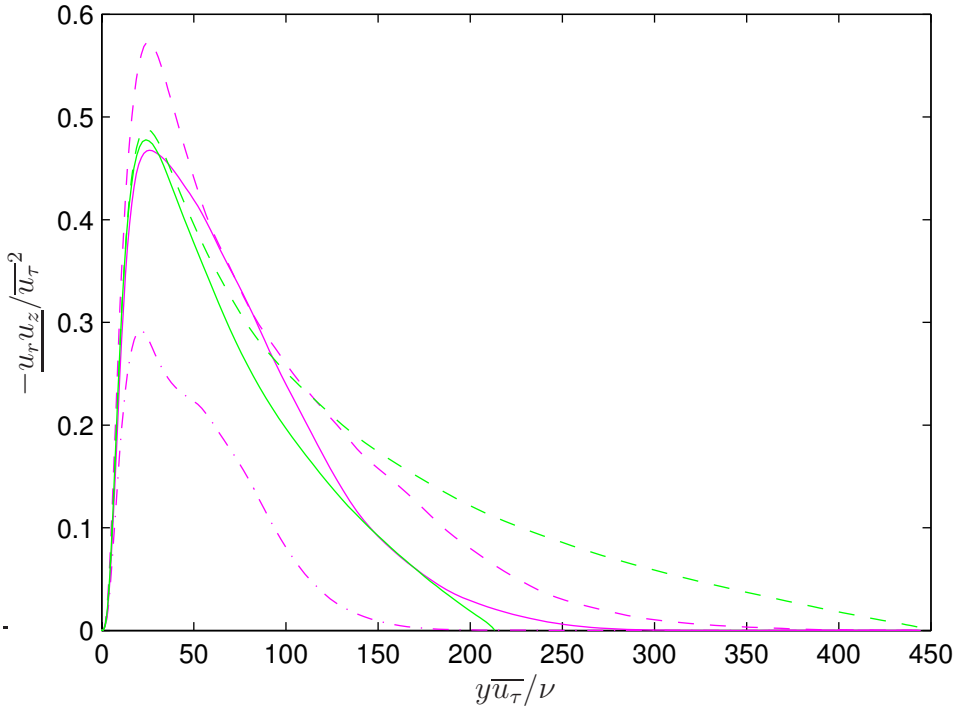

Figure 7.3: Reynolds shear-stress for flow case D2 ($\beta = 0.5°$, $Re_a = 674$, $\delta^*/a = 0.984$). Azimuthal positions: – – $\theta = 0$, —— $\theta = \pi/2$, – · – $\theta = \pi$. Axial flow at $Re_a = 674$: —— $b/a = 6$, – – $b/a = 12$.

windward side of the cylinder at most wall-normal positions. The profiles measured for the axial velocity component by Bücker and Lueptow [1998] show a similar trend to the present profiles (figure 7.4a) in the outer flow ($y\overline{u_\tau}/\nu \gtrsim 100$). However, unlike the present results, the measured profiles are nearly independent of azimuthal position near the wall ($y\overline{u_\tau}/\nu \lesssim 100$). The discrepancy may be due to the different Reynolds numbers used for the experiment and the simulation ($Re_a = 2600$ and 674 respectively).

RMS vorticity fluctuations are shown in figure 7.5. Once again, the yawed-flow profiles are higher on the leeward side and lower on the windward side of the cylinder relative to the profile at $\theta = \pi/2$, which is similar to the axisymmetric profiles near the wall ($y\overline{u_\tau}/\nu \lesssim 100$). Unlike the axisymmetric profiles, the yawed-flow profiles do not exhibit distortion near the outer boundary of the computational domain. This is because the axial-flow results correspond to the statistically-steady state, whereas the results for yawed flow are for temporally developing flows with little vorticity near the outer boundary.

Profiles of RMS pressure fluctuations are shown in figure 7.6. The "ripples" in the profiles suggest that a larger record of simulation data may be needed for the calculation of reliable pressure statistics. Even so, there are some consistent trends

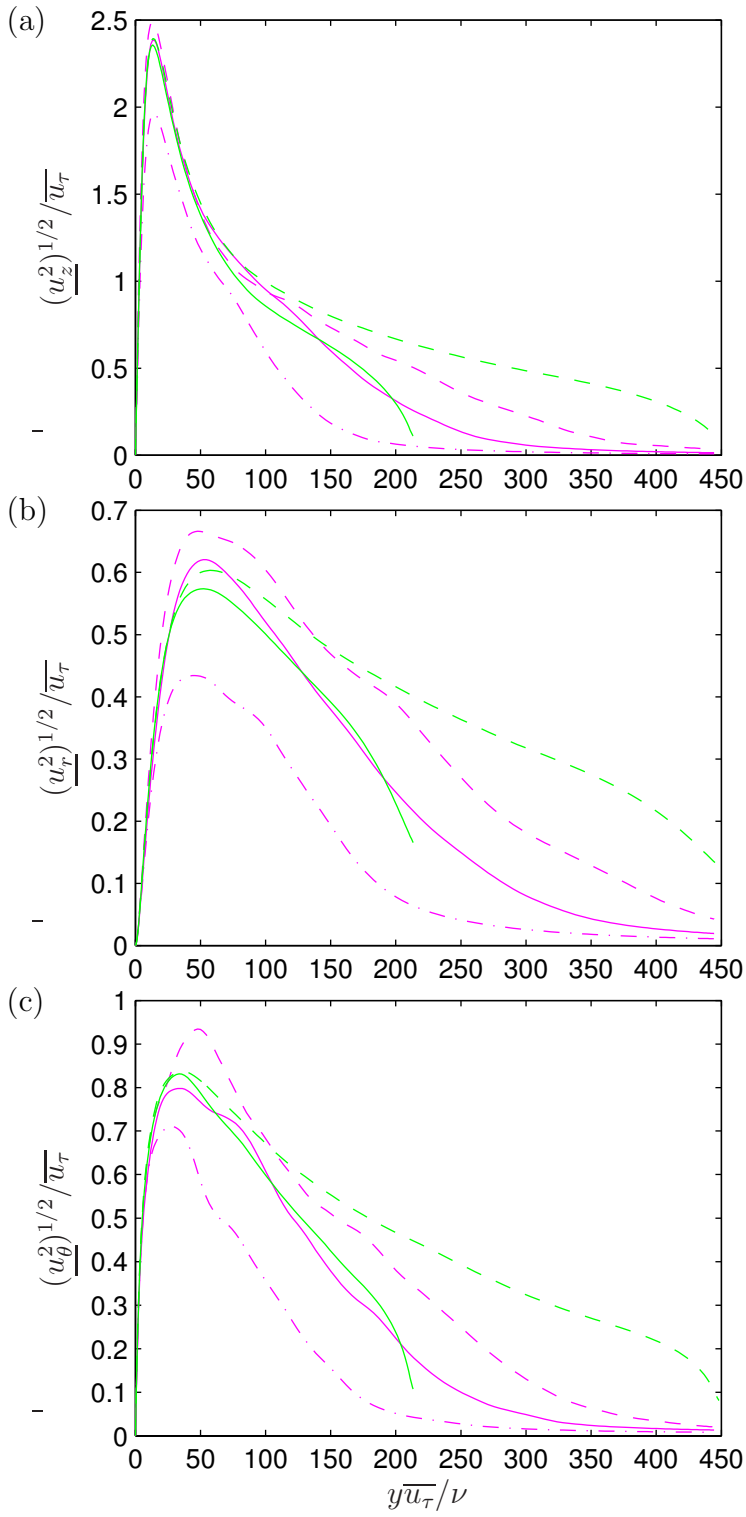

Figure 7.4: RMS velocity fluctuations for flow case D2 ($\beta = 0.5°$, $Re_a = 674$, $\delta^*/a = 0.984$). Velocity components: (a) axial, (b) radial, (c) azimuthal. Azimuthal positions: – – $\theta = 0$, —— $\theta = \pi/2$, ·–·– $\theta = \pi$. Axial flow at $Re_a = 674$: —— $b/a = 6$, – – $b/a = 12$.

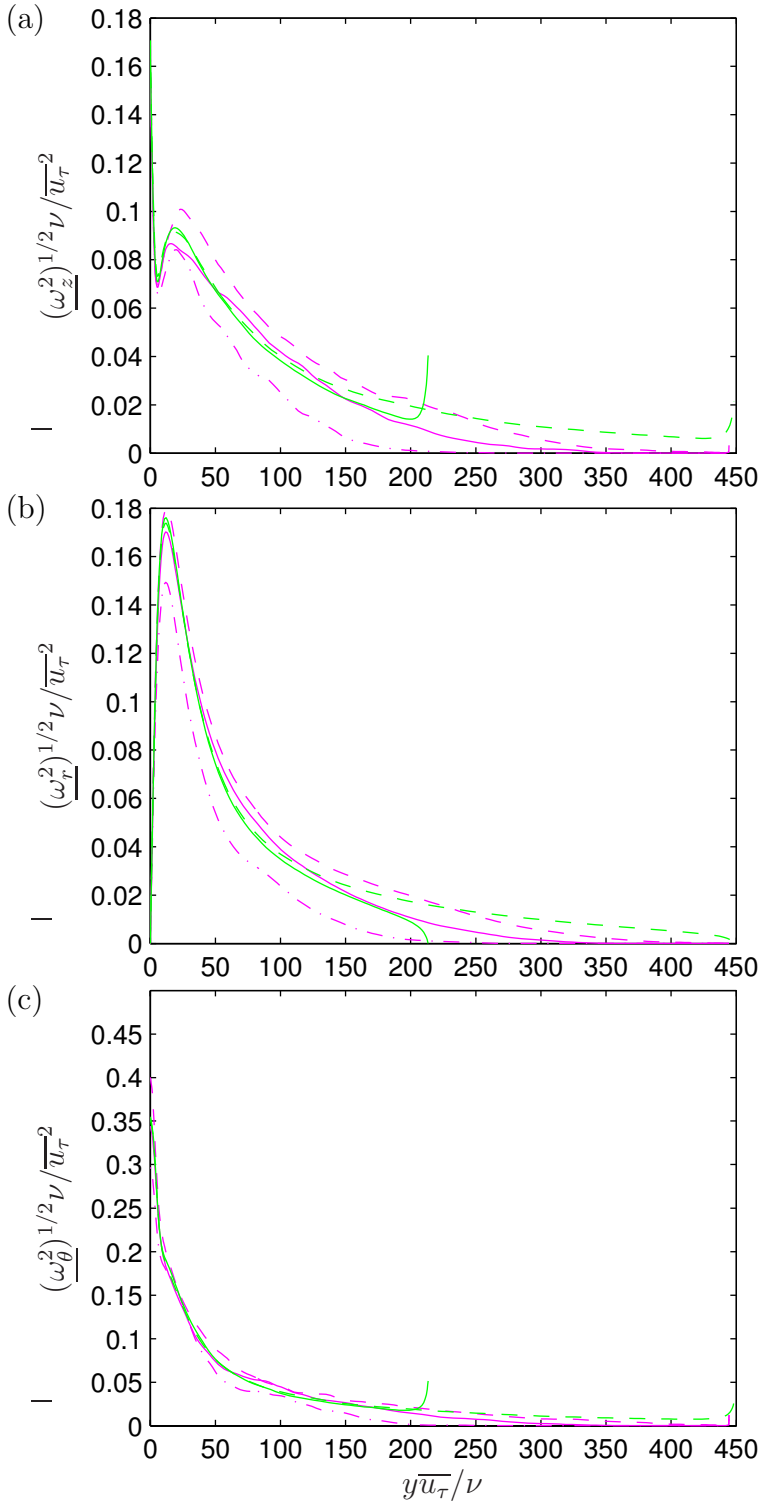

Figure 7.5: RMS vorticity fluctuations for flow case D2 ($\beta = 0.5°$, $Re_a = 674$, $\delta^*/a = 0.984$). Vorticity components: (a) axial, (b) radial, (c) azimuthal. Azimuthal positions: – – $\theta = 0$, —— $\theta = \pi/2$, · – · – $\theta = \pi$. Axial flow at $Re_a = 674$: —— $b/a = 6$, – – $b/a = 12$.

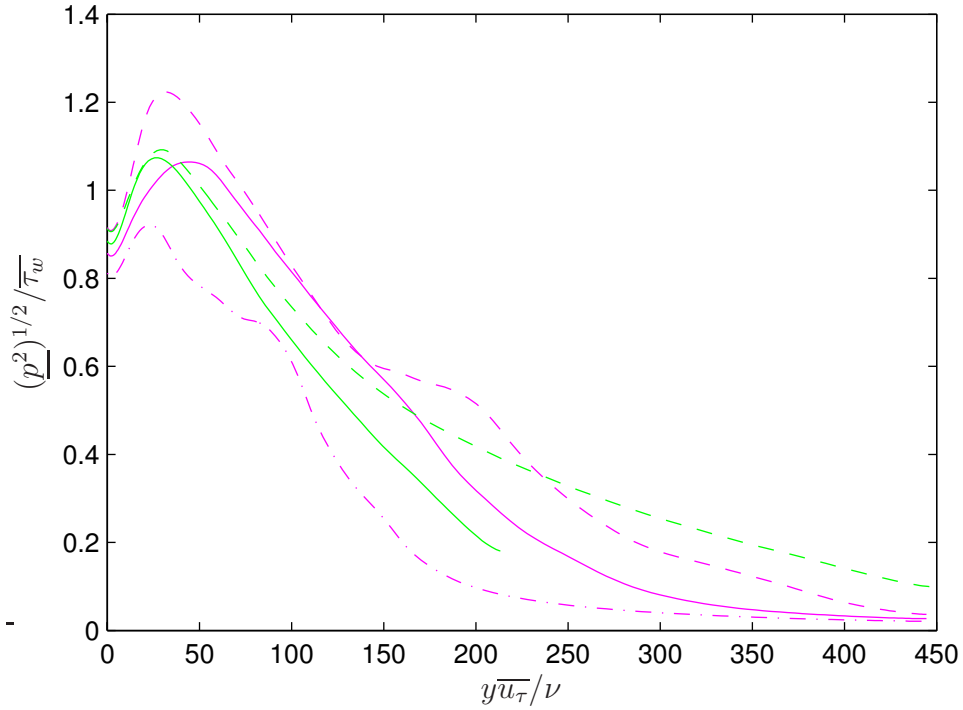

Figure 7.6: Profiles of RMS pressure for flow case D2 ($\beta = 0.5°$, $Re_a = 674$, $\delta^*/a = 0.984$). Azimuthal positions: – – $\theta = 0$, —— $\theta = \pi/2$, – · – $\theta = \pi$. Axial flow at $Re_a = 674$: —— $b/a = 6$, – – $b/a = 12$.

in the data. The profile for the leeward side of the cylinder is higher and that for the windward side is lower than the profile for $\theta = \pi/2$. The difference between the profiles for different azimuthal positions is smaller at the wall than elsewhere. The difference between the RMS wall-pressures on the leeward and windward sides of the cylinder is of the opposite sign to that found experimentally by Willmarth et al. [1977] and Berera [2004]. The discrepancy may be due to the much higher Reynolds numbers of the measured flows (Berera [2004]: $Re_a \approx 3300$; Willmarth et al. [1977]: $Re_a \gtrsim 3 \times 10^4$).

The plausible results produced by the present simulation procedure suggest that the numerical scheme is suitable for use in future investigations of turbulent boundary layers on cylinders in near-axial flow. The calculation of flow statistics may be improved, however, by use of ensemble averages instead of the azimuthal and temporal averages used for the present work. Data for the ensemble averages may be taken from corresponding time-steps of several simulations of the same flow case, with initial conditions for each simulation taken from different time-steps of an axial-flow simulation.

7.1.4 Instantaneous Flow Fields

Instantaneous flow fields are presented here for slices of flow case D2, which has $\beta = 0.5°$, $Re_a = 674$ and $\delta^*/a = 0.984$. To simplify comparison of different views, the contour levels and colour scales are consistent across all slices and vector components of a given flow variable (velocity or pressure). The in-plane motion of structures in the velocity field is represented by small arrows, whose sizes and directions are proportional to the local velocity vector.

Instantaneous velocity fluctuations ($\boldsymbol{U} - \underline{\boldsymbol{U}}$) on a transverse ($X$-$Y$) slice of the flow are shown in figure 7.7. There is considerable asymmetry in the distribution of structures around the cylinder. The region of flow that contains perceptible velocity fluctuations extends further from the cylinder on the leeward side than on the windward side. This observation is consistent with the RMS velocity profiles discussed previously. Coherent regions of the fluctuating axial velocity (figure 7.7a) appear to be fewer in number and larger in size on the windward side than on the leeward side. For the axial position shown, there are no significant regions of radial or azimuthal velocity (figures 7.7b,c) on the windward side.

Velocity fluctuations are visualised in figures 7.8–7.10 on a slice that includes the cylinder axis and is aligned with the free-stream velocity vector: the X-z plane. As before, the distribution of flow structures is clearly asymmetrical. The degree of asymmetry is greater than might be expected intuitively for such a small free-stream yaw angle. For the axial component of velocity (figure 7.8), the flow structures on the leeward side of the cylinder appear to be strongly mixed and broken into a range of sizes, whereas on the windward side, the large size of most of the structures suggests that there is little mixing of the fluid. For the radial and azimuthal components of velocity (figures 7.9 and 7.10), the sparse distribution of structures on the windward side suggests that turbulence is intermittent there. Such intermittency is not found on the leeward side of the cylinder or in axial flow at the same Re_a.

Velocity fluctuations are shown in figure 7.11 on an unwrapped, cylindrical slice (θ-z plane) of the flow at $y^+ = 15$. At this near-wall position, the streaky structure of the axial velocity component (figure 7.11a) appears to be unaffected by the free-stream yaw angle. Radial motion of fluid (figure 7.11b) is less common on the windward side ($r^+\theta \approx 175$) than on the leeward side of the cylinder. The streaks of azimuthal velocity (figure 7.11c) appear to be weaker and broader on the windward side than elsewhere. These features of the radial and azimuthal velocity components are consistent with the intermittency of turbulence noted above.

Wall-pressure fluctuations ($P - \underline{P}$) are shown in figure 7.12 on the unwrapped surface of the cylinder. The asymmetry of the wall-pressure is less pronounced

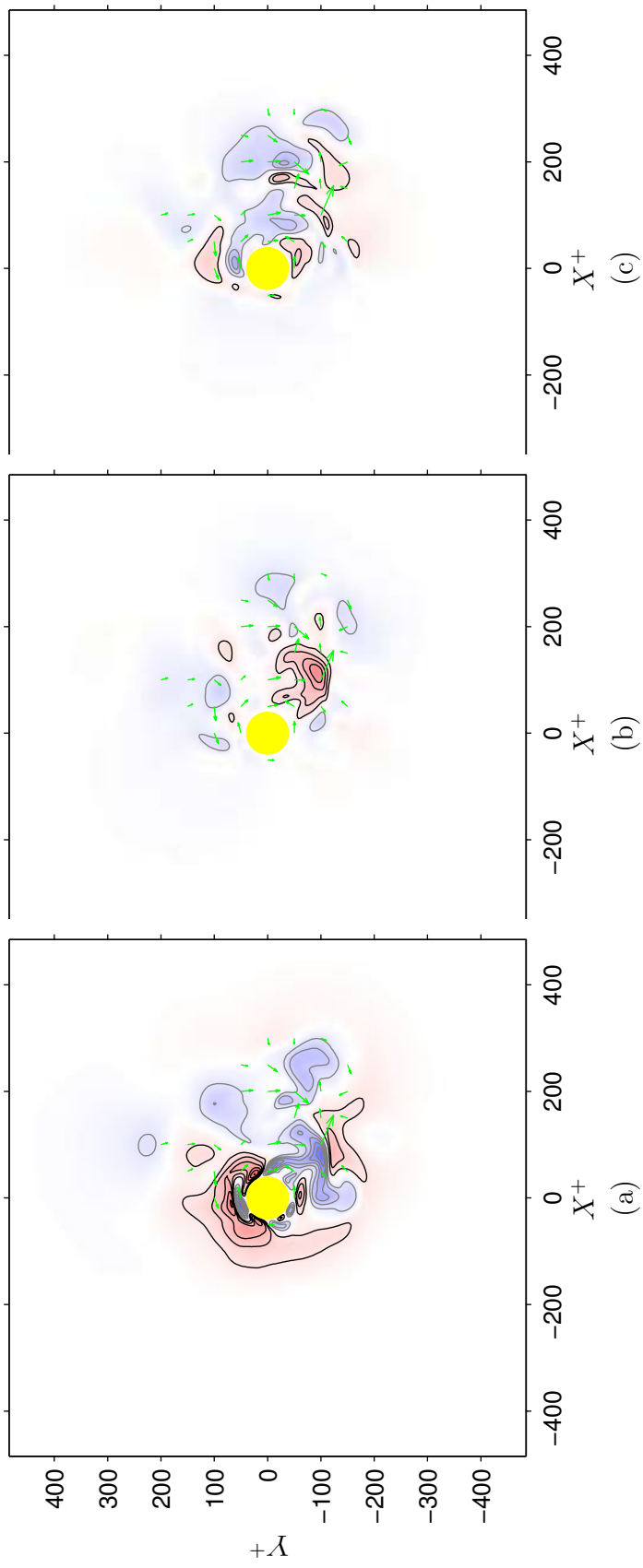

Figure 7.7: Instantaneous velocity fluctuations in plane $z^+ = 1250$ for case D2 ($\beta = 0.5°$, $Re_a = 674$, $\delta^*/a = 0.984$). Components: (a) axial, (b) radial, (c) azimuthal. Green arrows depict relative magnitude and direction of in-plane velocity. The contour increment is $0.6\,\overline{u_\tau}$. Black contours and red shading indicate $u_{r,\theta,z} > 0$, grey contours and blue shading indicate $u_{r,\theta,z} < 0$.

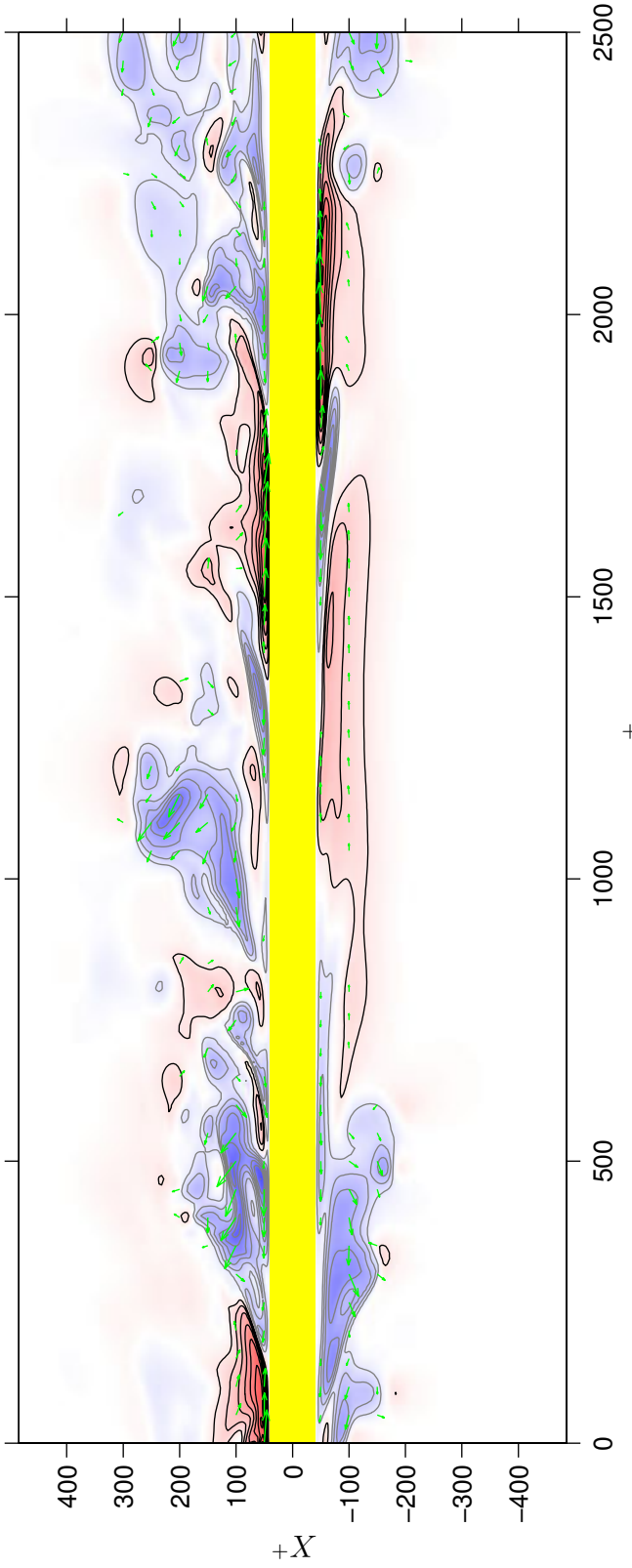

Figure 7.8: Instantaneous axial velocity fluctuations in plane $Y = 0$ for case D2 ($\beta = 0.5°$, $Re_a = 674$, $\delta^*/a = 0.984$). Green arrows depict relative magnitude and direction of in-plane velocity. The contour increment is $0.6\,\overline{u_\tau}$. Black contours and red shading indicate $u_z > 0$, grey contours and blue shading indicate $u_z < 0$.

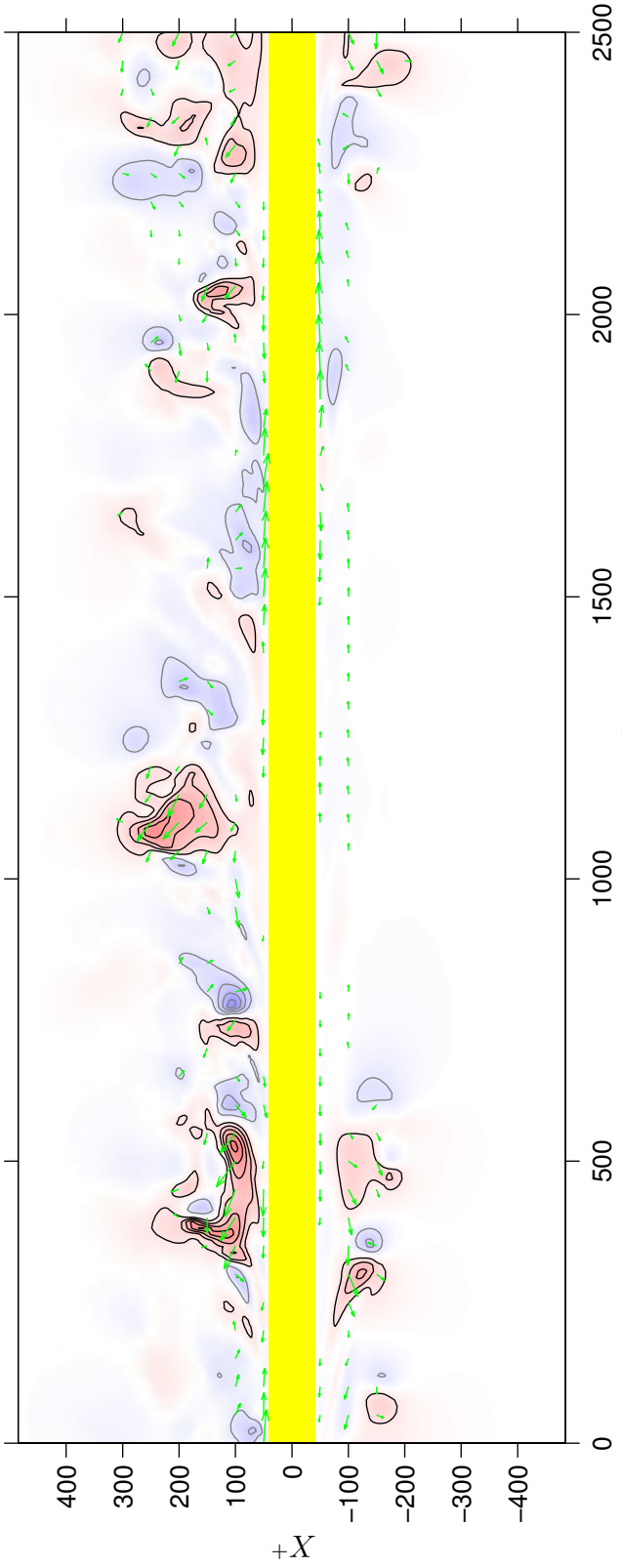

Figure 7.9: Instantaneous radial velocity fluctuations in plane $Y = 0$ for case D2 ($\beta = 0.5°$, $Re_a = 674$, $\delta^*/a = 0.984$). Green arrows depict relative magnitude and direction of in-plane velocity. The contour increment is $0.6\,\overline{u_\tau}$. Black contours and red shading indicate $u_r > 0$, grey contours and blue shading indicate $u_r < 0$.

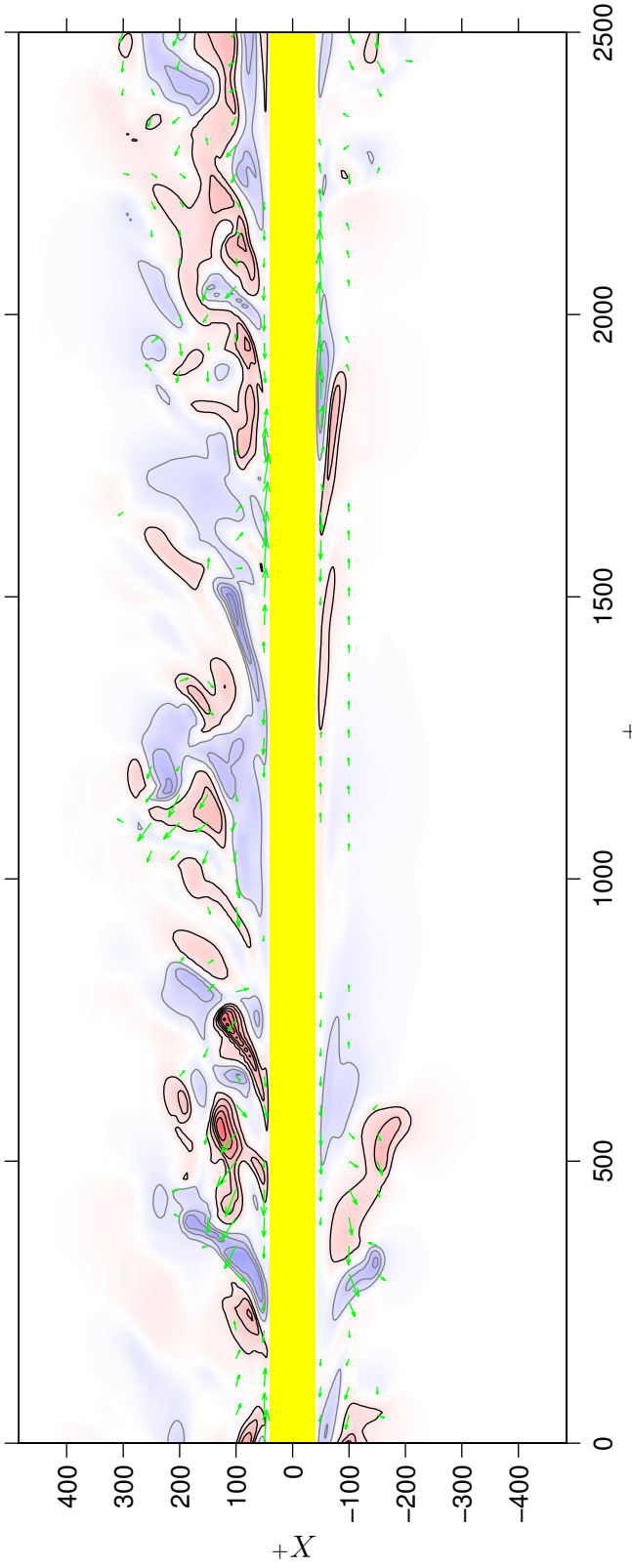

Figure 7.10: Instantaneous azimuthal velocity fluctuations in plane $Y = 0$ for case D2 ($\beta = 0.5°$, $Re_a = 674$, $\delta^*/a = 0.984$). Green arrows depict relative magnitude and direction of in-plane velocity. The contour increment is $0.6\,\overline{u_\tau}$. Black contours and red shading indicate $u_\theta > 0$, grey contours and blue shading indicate $u_\theta < 0$.

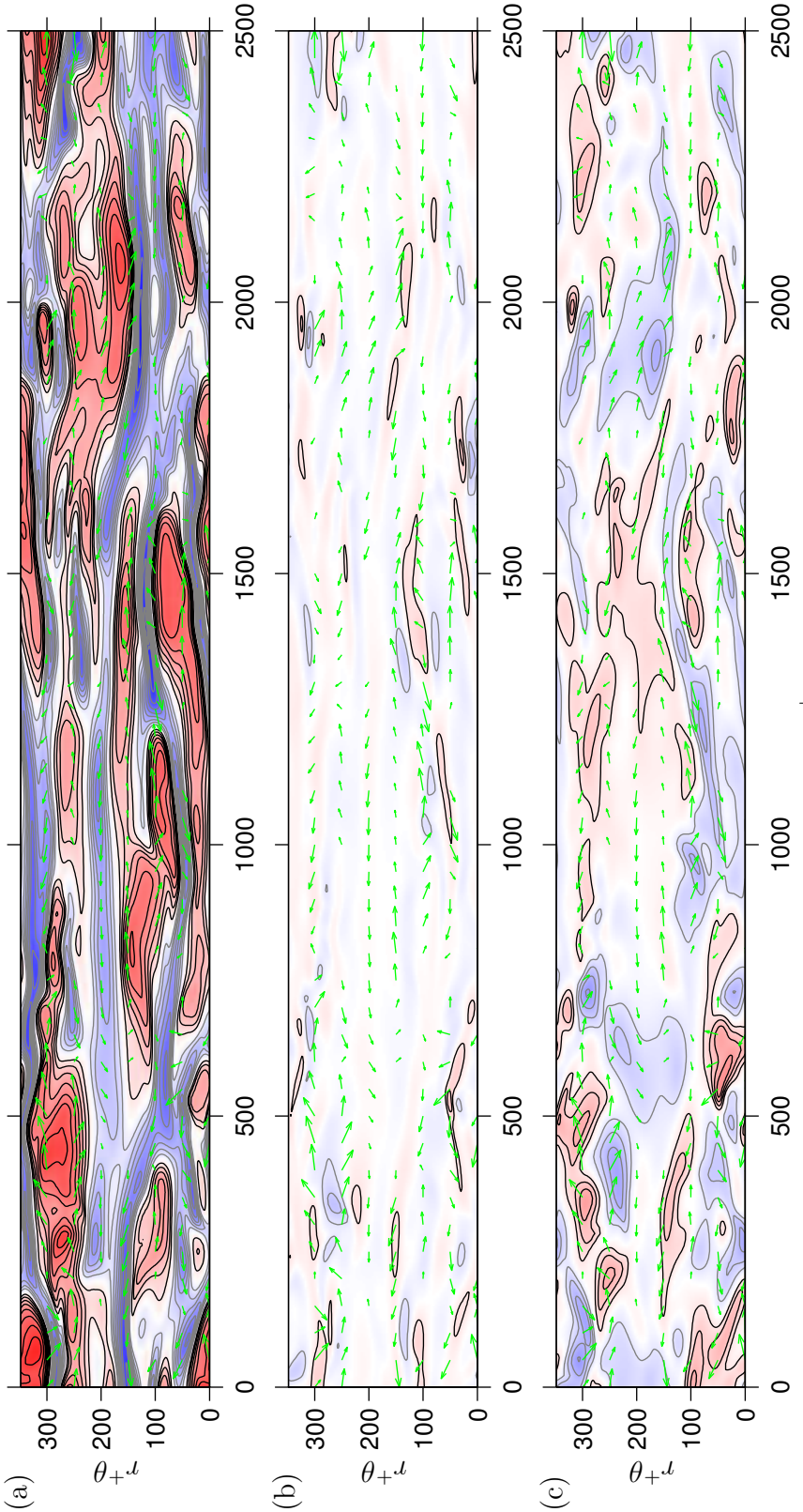

Figure 7.11: Instantaneous velocity fluctuations at $y^+ = 15$ for case D2 ($\beta = 0.5°$, $Re_a = 674$, $\delta^*/a = 0.984$). Components: (a) axial, (b) radial, (c) azimuthal. Green arrows depict relative magnitude and direction of in-plane velocity. The contour increment is $0.6\,\overline{u_\tau}$. Black contours and red shading indicate $u_{r,\theta,z} > 0$, grey contours and blue shading indicate $u_{r,\theta,z} < 0$.

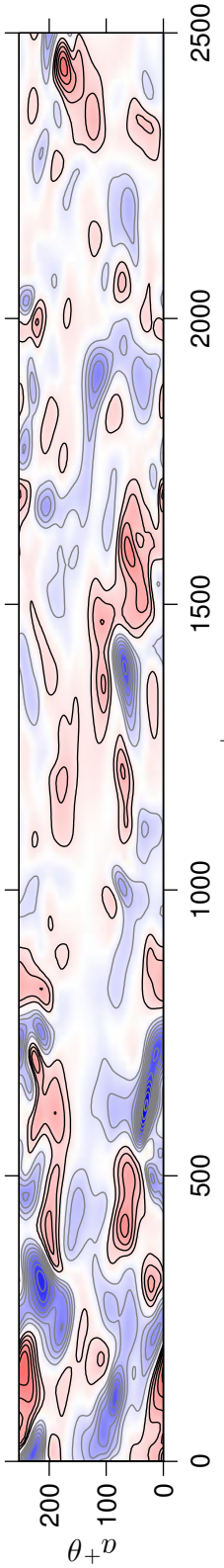

Figure 7.12: Instantaneous wall-pressure fluctuations for case D2 ($\beta = 0.5°$, $Re_a = 674$, $\delta^*/a = 0.984$). The contour increment is $0.5\,\overline{\tau_w}$. Black contours and red shading indicate $p > 0$, grey contours and blue shading indicate $p < 0$.

than the asymmetry of the velocity fluctuations. This is because the wall-pressure includes contributions from pressure-sources distributed throughout the boundary layer, as discussed in section 5.2. The asymmetry of the pressure-source distribution, which reflects that of the underlying velocity field, is masked to some extent when the contributions of the pressure-sources are combined at the wall.

7.2 Vortex-Shedding in Near-Axial Flow

The experiments of Bull and Dekkers [1993a] show that a form of vortex-shedding occurs when the yaw angle β exceeds a threshold that depends on the Reynolds number Re_a. The vortices appear to be shed at an angle to the cylinder, with one end remaining attached to and travelling along the cylinder.

To investigate this phenomenon further, a simulation of flow with $\beta = 3°$ and $Re_a = 311$ was performed. These parameters are within the range identified by Bull and Dekkers [1993a] for which vortex-shedding is measured. The mesh geometry used for the simulation corresponds to that listed in table 3.1 for the axial-flow simulation with $Re_a = 311$ and $b/a = 21$. Initial conditions for the yawed-flow simulation were taken from the statistically-steady state of an unreported axial-flow simulation with $Re_a = 311$ and $b/a = 6$. The yawed-flow simulation was advanced over a time interval of duration $1500a/V_\infty$, to allow the initially turbulent boundary layer to develop into vortex-shedding flow. The end of the development phase is denoted by $t = 0$. The simulation was continued to time $t = 250a/V_\infty$, and the flow fields were saved periodically (at increments of $t = a/V_\infty$) to establish the data record presented here.

Figure 7.13a shows the axial component of velocity (U_z/V_∞) as a function of time (tV_∞/a) at a fixed axial position ($z = 0$). The six traces correspond to two different azimuthal positions ($\theta = 0, \pi/4$) and three different wall-normal positions ($y/a = 0.2, 1, 5$). Each time-series features continuous oscillations with a constant period. The amplitude of the oscillations is not constant, suggesting either that a longer simulation time may be required to achieve regularity or that the selected flow case may be in a transitional state between laminar vortex-shedding and turbulence. The temporal period of the oscillations ($25a/V_\infty$) is independent of wall-normal position and, hence, local mean velocity.

The oscillation frequency at the centre of the wake ($\theta = 0$) is exactly double that for off-centre locations (for example, at $\theta = \pi/4$). The measurements of Bull and Dekkers [1993a] are for an off-centre location. They report that the shedding frequency is constant along the length of the cylinder if the free-stream velocity

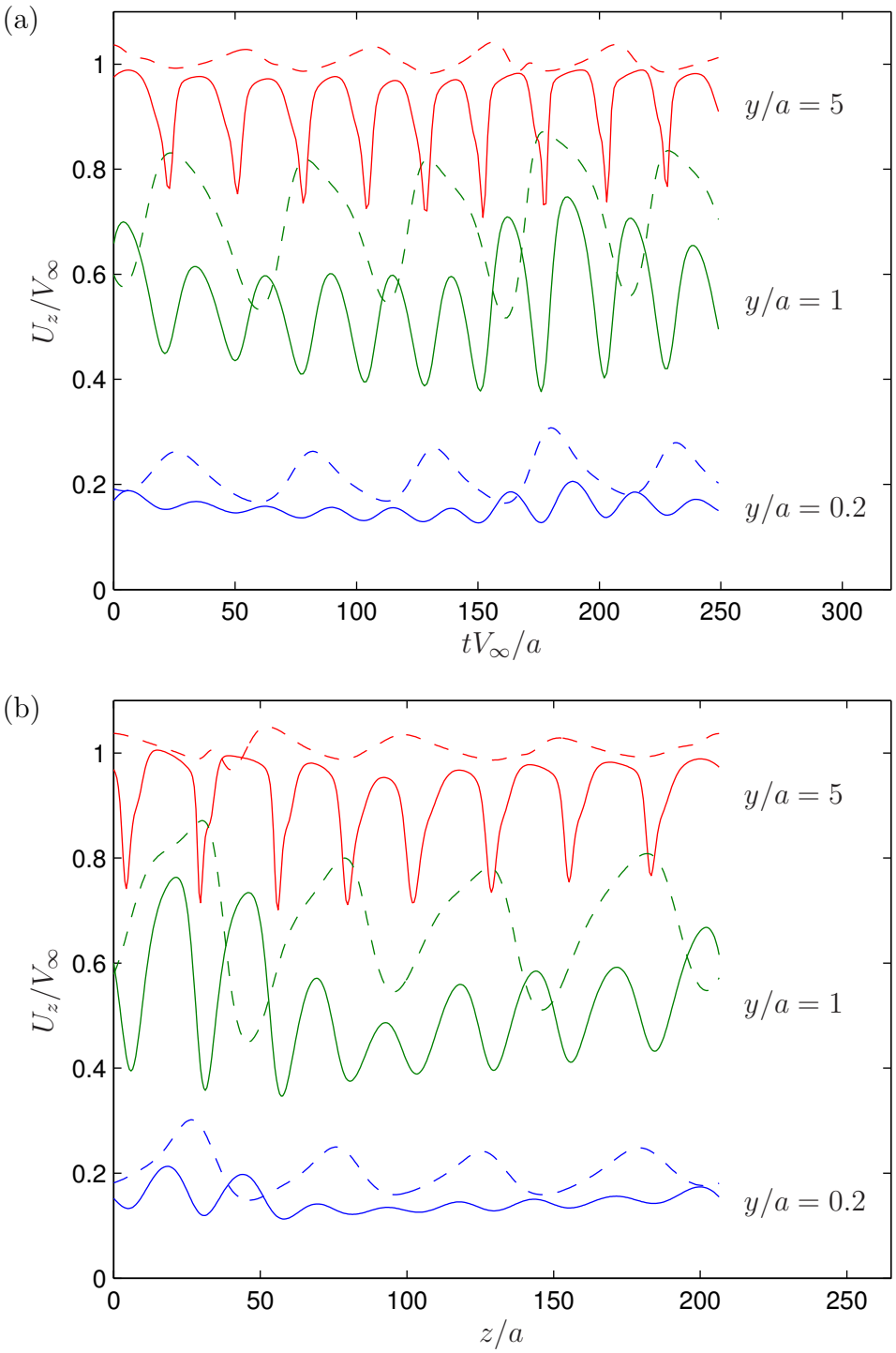

Figure 7.13: Axial velocity in vortex-shedding near-axial flow ($\beta = 3°$, $Re_a = 311$, $b/a = 21$) as a function of (a) time and (b) axial position. Traces are shown for azimuthal positions $\theta = 0$ (solid lines) and $\theta = \pi/4$ (dashed lines) and wall-normal positions $y/a = 0.2, 1, 5$ (as labelled). Temporal traces are for the axial position $z = 0$, and spatial traces are for time $t = 0$.

is uniform. This observation suggests that the simulation, despite the effectively infinite length of the cylinder, ought to produce the same shedding frequency as a comparable experiment. The simulated Strouhal number and frequency parameter (based on cylinder diameter) are, respectively, $St = 2fa/V_\infty = 0.039$ and $F = 4fa^2/\nu = 24$. These values are in respectable agreement with those obtained by interpolation of the experimental data of Bull and Dekkers [1993a] ($St \approx 0.03$, $F \approx 20$).

The axial component of velocity (U_z/V_∞) as a function of axial position (z/a) is plotted in figure 7.13b at time $t = 0$ for the same azimuthal and wall-normal positions as before. Data are shown for the full axial length of the computational domain, and it may be observed that the velocity values at $z/a = 0$ and 207 are equal due to the periodic boundary conditions. If the spatial waveforms in figure 7.13b were to move in the positive z-direction, the temporal variation observed at $z = 207$, and therefore at $z = 0$, would strongly resemble the temporal waveforms in figure 7.13a. Thus, the velocity oscillations have the character of a wave travelling in the axial direction. The propagation speed of the wave, given by the ratio of the spatial period ($25a$) and the temporal period ($25a/V_\infty$) of the oscillations, is equal to V_∞, or perhaps more correctly $V_{\infty z} = 0.999V_\infty$ (for $\beta = 3°$), regardless of the local velocity of the flow.

Velocity streamlines at time $t = 0$ are shown in figure 7.14. Also shown is the corresponding radial component of vorticity on a slice along the centre of the wake ($\theta = 0$). Vortex structures extend outwards from the cylinder into the wake — hence the classification "vortex-shedding". The streamlines in the wake are wave-like, with maximum curvature in the vicinity of the vortex structures. The vorticity slice is qualitatively similar to the hydrogen-bubble flow visualisations of Bull and Dekkers [1993a]. However, it is difficult to demonstrate quantitative agreement of parameters such as the yaw angles of the vortex structures. The reason for this may be that the streaklines formed by the passage of fluid over a bubble-wire are typically quite different from streamlines and other visualisations of instantaneous fields in an unsteady, time-varying flow.

The instantaneous vorticity field at time $t = 0$ is visualised in figure 7.15 by means of vortex lines (vorticity streamlines) and isosurfaces of vector components. The vortex lines, which appear to form closed loops around the cylinder, are stretched towards the wake. The azimuthal orientation of the vorticity isosurfaces and vortex loops varies in a wave-like fashion along the length of the cylinder. The three-dimensional structure of the vorticity field suggests that the classification

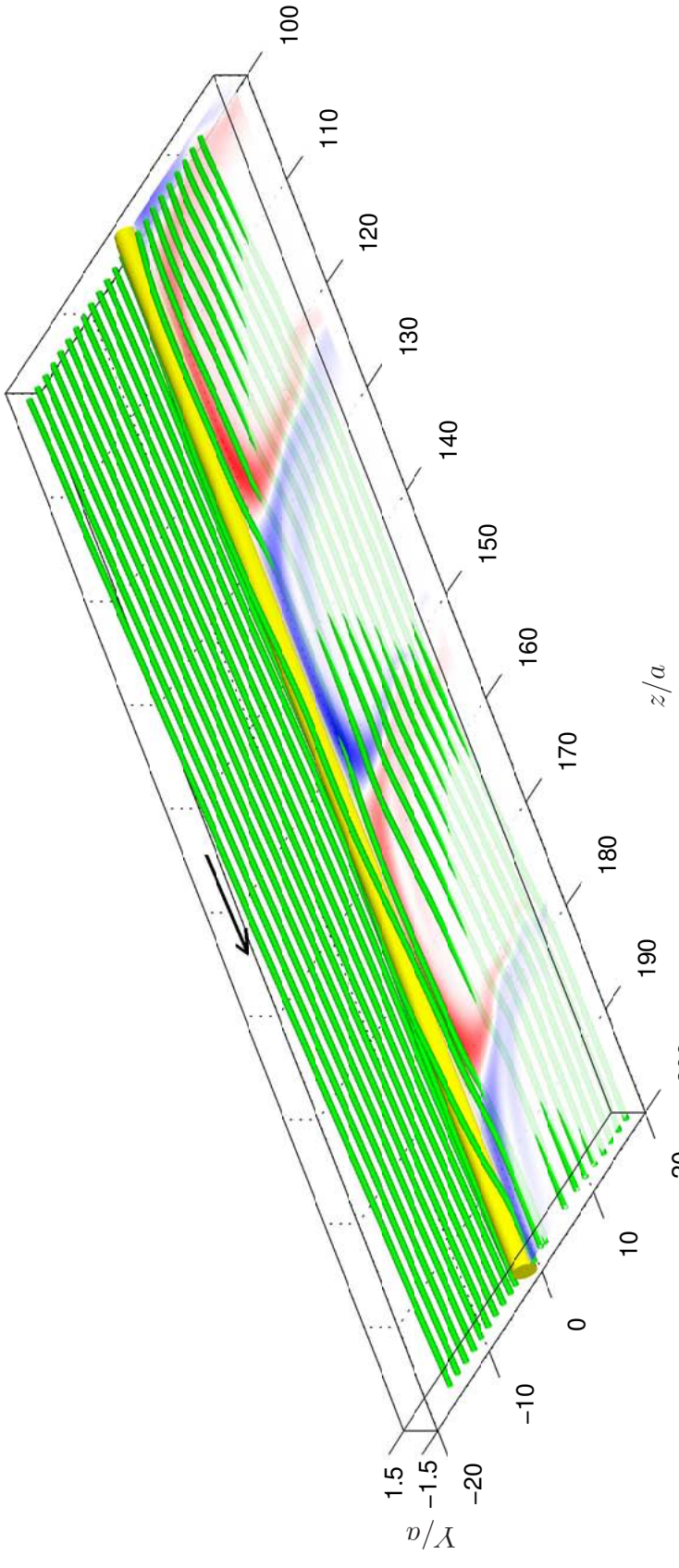

Figure 7.14: Instantaneous velocity for vortex-shedding near-axial flow ($\beta = 3°$, $Re_a = 311$, $b/a = 21$). Free-stream flow direction is marked by a black arrow. Starting positions for green streamlines lie on the line $(Y/a, z/a) = (0, 101)$ at multiples of $X/a = \pm 1.5a$. For reference, the radial component of vorticity in the plane $X > 0, Y = 0$ is shown on a transparent surface, where red and blue shading indicate, respectively, positive and negative ω_r.

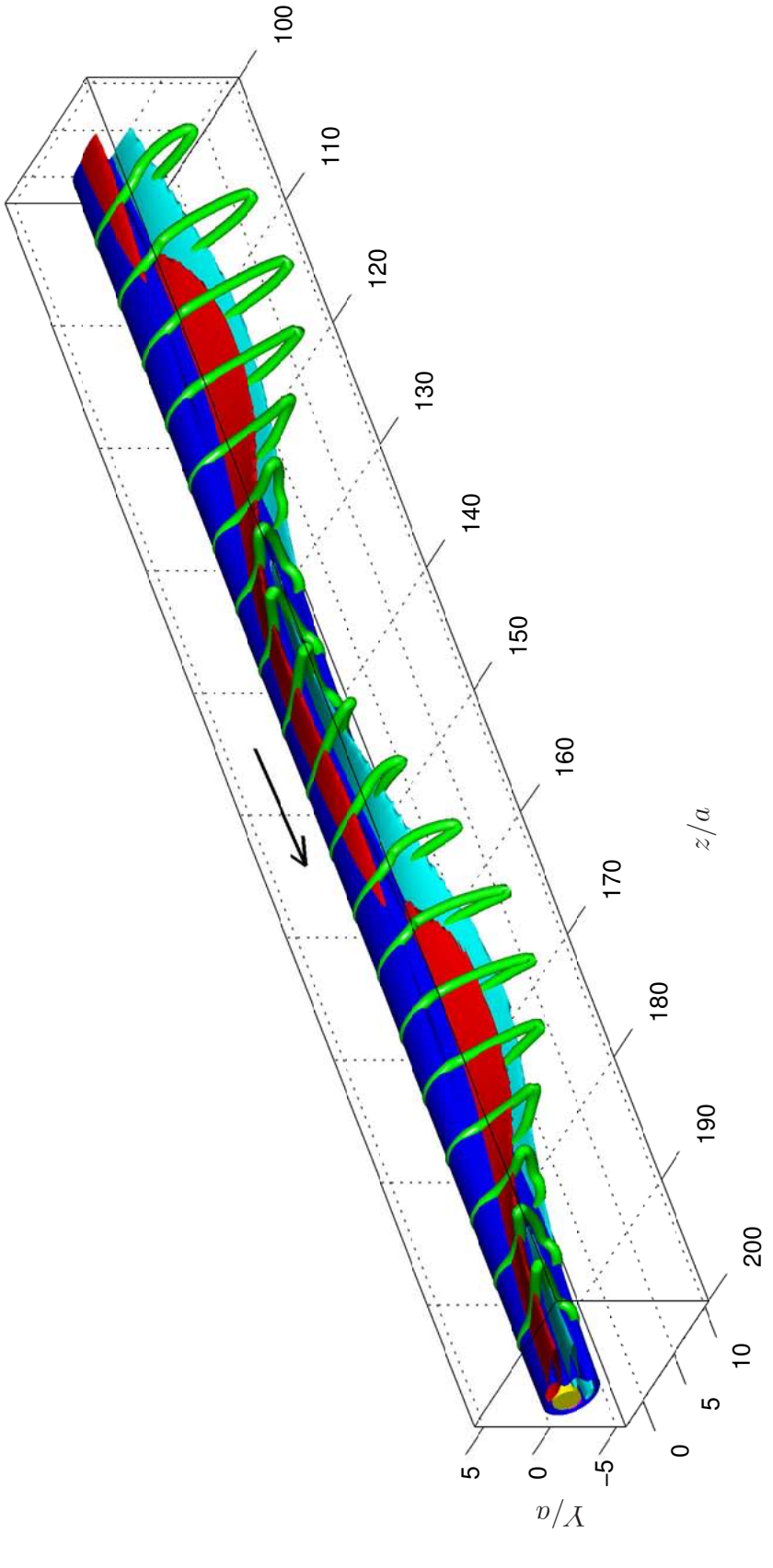

Figure 7.15: Instantaneous vorticity for vortex-shedding near-axial flow ($\beta = 3°$, $Re_a = 311$, $b/a = 21$). Free-stream flow direction is marked by a black arrow. Isosurfaces for $\Omega_{r,\theta,z} = \pm 0.25 V_\infty / a$ with visible components $\Omega_\theta < 0$ (blue), $\Omega_r > 0$ (red) and $\Omega_r < 0$ (cyan). Vortex lines passing through the line $(X/a, Y/a) = (-1.33, 0)$ are coloured green.

"vortex-shedding" is not strictly accurate, because individual vortex structures are observed only in two-dimensional slices of the flow.

Contours of the instantaneous wall-pressure field at time $t = 0$ are shown in figure 7.16. The maximum pressure occurs on the windward side of the cylinder, as expected. The location of minimum pressure alternates between the top and bottom of the cylinder over the length of the cylinder. The spatial variation of pressure corresponds to a time-varying local lift (in the Y-direction), which may excite transverse vibration of a flexible cylinder.

Early investigations of yawed flow over cylinders [see, for example, Chiu and Lienhard, 1967] invoke the so-called "independence principle", which is the notion that the components of free-stream velocity normal to and parallel with the cylinder may be regarded as independent. The experimental results of van Atta [1968], amongst others, indicate that the independence principle only holds for a limited range of yaw angles in the neighbourhood of cross-flow ($\beta \approx 90°$). In the present yawed-flow simulation, the Reynolds number normal to the cylinder, $aV_X/\nu \approx 16$, is so low that steady laminar flow would be expected for a cylinder in cross-flow. The fact that vortex-shedding occurs instead is further evidence that the independence principle is not valid at small yaw angles.

Although the influence of computational domain size on the present flow has not been investigated, the domain used here ($b/a = 21$, $L_z/a = 207$) is quite large in relation to the cylinder radius. Use of a larger domain may lead to quantitative changes in the flow, but it is considered unlikely that qualitative features such as the general structure of the flow would be dramatically affected.

7.3 Summary and Conclusions

The simulation procedure described in chapter 2 has been applied to flows with the free-stream inclined at an angle β to the cylinder axis. Simulations of turbulent boundary layers have been performed for several yaw angles ($\beta = 0.25°, 0.5°$), Reynolds numbers ($Re_a = 311,674$) and displacement thicknesses ($\delta^*/a < 1.3$). The lack of axisymmetry in yawed flow implies that the outer radial boundary of the cylindrical computational domain may cause truncation and distortion of the flow on the leeward side of the cylinder in simulations of yawed flow produced by the present procedure. To avoid this problem, data are collected from simulations of turbulent yawed flow after a suitable development time but before significant vorticity accumulates near the outer domain boundary. The lack of both statistical steadiness and axisymmetry makes it necessary to average statistics over small

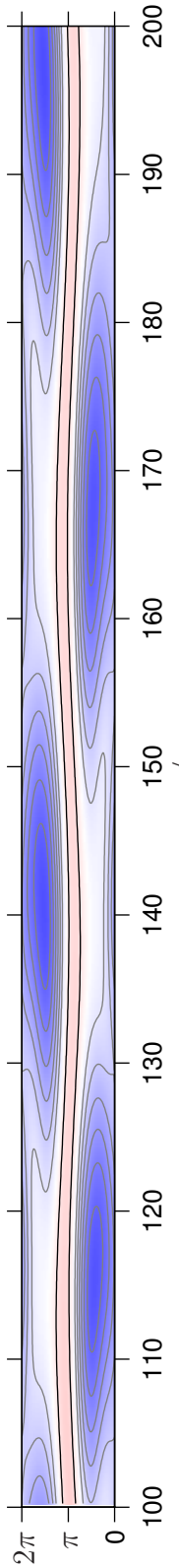

Figure 7.16: Instantaneous wall-pressure for vortex-shedding near-axial flow ($\beta = 3°$, $Re_a = 311$, $b/a = 21$). Contour increment is $0.001\rho V_\infty^2$. Black contours and red shading indicate $P > 0$, grey contours and blue shading indicate $P < 0$.

temporal and azimuthal intervals, in addition to averaging over the axial length of the domain.

Contours of mean velocity indicate that the mean flow is characterised by values of β, Re_a and δ^*/a and is little affected by the initial conditions used for simulation after a sufficient development time has elapsed. As Re_a increases, the width of the contours in the direction normal to the plane of the free-stream (the Y-direction) increases so that the contours become more circular. As the yaw angle increases, contours move closer to the cylinder on the windward side and further away on the leeward side.

Mean velocity profiles in wall units, based on the azimuthally averaged friction velocity $\overline{u_\tau}$, are higher on the windward side and lower on the leeward side of the cylinder. In the logarithmic region, the yawed-flow profiles are shifted upwards or downwards depending on azimuthal position, but the slope of the profiles is nearly independent of azimuthal position and is very similar to that of the logarithmic region in axisymmetric flow with the same value of Re_a.

Profiles of yawed-flow turbulence statistics, including Reynolds shear-stress, RMS velocity, RMS vorticity and RMS pressure, when plotted in wall units based on $\overline{u_\tau}$, are lower on the windward side and higher on the leeward side of the cylinder, which is the opposite of the trend noted for the mean velocity profiles. The difference between the RMS wall-pressures on the leeward and windward sides of the cylinder is of the opposite sign to that found experimentally by Willmarth et al. [1977] and Berera [2004]. The discrepancy may be due to differences between the flow regimes in the simulations and experiments. The values of Re_a used for the present simulations are sufficiently low that the turbulence appears to be intermittent on the windward side of the cylinder, as indicated by the sparse distribution of structures in the instantaneous radial velocity field, for example. In contrast, the Reynolds numbers considered in the experiments (3300 and larger) almost certainly correspond to fully turbulent flow.

An additional simulation has been performed with the parameters $\beta = 3°$, $Re_a = 311$ and $b/a = 21$. The simulation has been advanced in time sufficiently to allow the initial condition, an axisymmetric, turbulent boundary layer, to develop into vortex-shedding flow of the kind observed experimentally by Bull and Dekkers [1993a]. In such a flow, the vortices appear to be shed at an angle to the cylinder, with one end remaining attached to and travelling along the cylinder.

Plots of the axial component of velocity as functions of either time or axial position feature continuous oscillations with a uniform temporal or spatial period. The velocity oscillations have the character of a wave travelling in the axial direction

(towards increasing z) with a propagation speed equal to V_∞, or perhaps more correctly $V_{\infty z}$, regardless of the local velocity of the flow.

Vortex lines appear to form closed loops around the cylinder and are stretched towards the wake. The azimuthal orientation of the vortex loops varies in a wave-like fashion along the length of the cylinder. The three-dimensional structure of the vorticity field suggests that the classification "vortex-shedding" is not strictly accurate, because individual vortex structures are observed only in two-dimensional slices of the flow. However, the term vortex-shedding is used here for consistency with the existing literature on the subject.

The spatial variation of wall-pressure corresponds to a time-varying local lift in the direction normal to the plane of the flow (the Y-direction), which may excite transverse vibration of a flexible cylinder.

The present simulation for $\beta = 3°$ shows that the occurrence of vortex-shedding in near-axial flow is not directly determined by the normal component of the free-stream velocity (V_X), as assumed by the so-called "independence principle". In fact, the Reynolds number normal to the cylinder ($aV_X/\nu \approx 16$) is so low that steady laminar flow would be expected for a cylinder in cross-flow. The simulation also demonstrates that vortex-shedding is possible in the absence of cylinder vibration or specific end-effects, none of which are included in the computational model.

Chapter 8

Research Findings

8.1 Introduction

The present investigation concerns the simulation of time-varying, three-dimensional flow over a long circular cylinder that is aligned with or slightly inclined to the free-stream. Flows of this type remain relatively unexplored, compared with boundary layers on flat plates or cross-flow over cylinders, despite their common occurrence in engineering applications. An example of such a flow is the towed array sonar used for maritime surveillance and geophysical exploration, where a cylindrical tube containing a series of hydrophones is towed behind a ship or submarine. The surface shear stresses and pressure fluctuations associated with the flow of water over the surface of the array are directly relevant to the mechanical design of the array and its effectiveness in detecting weak acoustic signals. Numerical simulation of flows of this type is useful in supporting and clarifying conclusions deduced from experimental investigations, and in uncovering details of the flow that cannot be readily obtained by experiment.

In the initial part of this work, a numerical scheme is developed for solution of the governing Navier-Stokes equations. The scheme is similar to the pseudo-spectral method employed by Neves [1992], but here rather different boundary conditions are imposed at the outer radial limit of the cylindrical computational domain. A comparison of the present boundary conditions with those of Neves [1992] is given later in section 8.2. Irrespective of the outer boundary conditions used, the axial periodicity imposed on the cylindrical domain ensures that simulations reach a statistically-steady state after a sufficient calculation time.

The present work mainly concentrates on direct numerical simulations (DNS) of turbulent boundary layers in axial flow at the statistically-steady state. The flow conditions considered have radius Reynolds numbers in the range $Re_a = aV_\infty/\nu =$

311–20800, ratios of boundary layer thickness to cylinder radius in the range $\delta/a =$ 0.16–28, and boundary layer thickness in wall units covering the range $\delta^+ = \delta u_\tau/\nu =$ 160–800. These ranges considerably extend the available DNS data for axisymmetric boundary layers. Particular attention is given to the assessment of scaling laws for the mean velocity profile, velocity fluctuation statistics and temporal wall-pressure spectra. Structural features of the flow are examined by inspection of instantaneous flow fields and conditionally-averaged flow structures.

In the latter part of the thesis, attention is given to simulations of near-axial flow. No previous flow simulations of near-axial flow appear to have been reported in the literature. The numerical scheme used is the same as for axial flow, except that results are obtained before the simulations reach a statistically-steady state. Turbulent flows are considered with $Re_a = 311$ and 674 and yaw angles of 0.25 and 0.5 degrees. The effects of the yaw angle on flow statistics and instantaneous structures are explored. Finally, the yaw angle for flow at $Re_a = 674$ is increased to 3 degrees, and the structure of the resulting vortex-shedding flow is inspected.

A summary of the main findings of the investigation is presented in the following sections.

8.2 Simulation Boundary Conditions

The principal difference between the computational method used for the present axial-flow simulations and that used by Neves [1992] is the boundary condition imposed at the outer radial limit of the cylindrical domain.

In the method used by Neves, the outer boundary condition is imposed on the velocity field. The radial velocity component is explicitly set to zero, and the azimuthal and axial velocity components are set so that the shear stress is zero at the outer edge of the domain. Neves [1992, p. 12] asserts that the specified boundary conditions prevent the occurrence of large-scale viscous/inviscid interactions, so that the computational method is incapable of capturing large-scale cross-flow events of the kind observed experimentally by Lueptow and Haritonidis [1987].

The outer boundary condition used for the present simulations is designed to accommodate large-scale cross-flow events. The boundary condition also allows the simulation procedure to accommodate a free-stream that is yawed relative to the cylinder axis. For these purposes, the outer boundary condition is imposed on the vorticity field. Specifically, the radial component of vorticity is set to zero and the remaining components are determined so that the resultant magnitude of the vorticity vector is minimised. The vorticity field is confined to the computational

domain, while the velocity field is assumed to be continuous throughout space, with the external potential flow tending to the free-stream at infinity. Vorticity becomes the primary simulation variable, whose evolution is governed by the vorticity transport equation, and the velocity field is determined from the vorticity field at each time-step.

In chapter 4, the velocity statistics obtained for two flow cases by Neves [1992] are compared with the statistics produced by the present simulation procedure. For flows with corresponding values of the Reynolds number Re_a and domain size b/a, the velocity statistics produced by the two methods are nearly indistinguishable near the cylinder wall. The effects of the different boundary conditions are most noticeable near the outer boundary of the computational domain. In particular, the radial component of RMS velocity decays to zero in the results of Neves, whereas in the present results, the radial velocity is allowed to be non-zero at the outer boundary.

There is no suggestion in the velocity statistics that the velocity boundary conditions used by Neves suppress any of the essential physical processes at work near the cylinder wall. For the simulation of axisymmetric boundary layers, there appears to be little reason to prefer the vorticity boundary conditions used here over the more straight-forward velocity boundary conditions used by Neves. For simulations of yawed flow, however, the vorticity boundary conditions have the advantage that they allow the present simulation procedure to take account of the free-stream yaw angle and the displacement of the external potential flow by the time-varying boundary layer.

8.3 Turbulent Cross-Flow Events

Luxton et al. [1984] report on experimental measurements of skewness and flatness profiles for a set of axisymmetric boundary layers with large δ/a. The differences between profiles for axisymmetric and planar boundary layers led Luxton et al. to suggest that the mechanisms of turbulence generation may be different in boundary layers on cylinders compared with those on plane surfaces. It was hypothesised that the turbulence generation mechanisms in axisymmetric boundary layers with large δ/a are enhanced by the motion of large-scale turbulence structures across the cylinder.

Lueptow and Haritonidis [1987] describe experimental visualisations of axial flow over a cylinder, in which they observed large-scale structures moving from one side of the cylinder to the other. Evidence for the occurrence of large-scale cross-flows

is also found in the results of the present axial-flow simulations, as discussed in section 6.1 where slices of instantaneous flow fields are displayed. Neves [1992, p. 4] suggests that the experimentally observed cross-flow events may have been caused by vibration of the cylinder. However, some of the evidence for the occurrence of cross-flow events has been obtained from experiments in which efforts were made to minimise vibration of the cylinder, as was the case for Luxton et al. [1984]. The present simulations confirm that large-scale cross-flows can occur without vibration of the cylinder, because the simulation procedure is based on a computational model which assumes that the cylinder is rigid.

The occurrence of large-scale cross-flows in the present simulations is most apparent when a^+ is small and δ/a is large. In such a situation, there is typically a small number of flow structures distributed around the cylinder at a given streamwise location, and many of the structures are significantly larger than the cylinder cross-section. At irregular intervals along the cylinder, the structures can be expected to interact in such a way that there is coherent motion of fluid across the cylinder. The large size of the structures relative to the cylinder ensures that the cross-flow motion is not inhibited by the cylinder wall.

The present simulations indicate that in axisymmetric boundary layers, including those where large-scale cross-flows are likely to occur, the mechanisms of turbulence generation are not fundamentally different from those in planar boundary layers. The quadrant analyses presented in section 4.6 suggest that Reynolds-stress generation mechanisms in axisymmetric boundary layers are essentially unchanged from planar flow, where cross-flow can never occur. The conditional averages presented in section 6.3 do not confirm a link found experimentally by Bull and Dekkers [1993b] between cross-flows and low-speed spots. The apparent link found by Bull and Dekkers may be due to the very low values of Re_a (160) and a^+ (~ 13) used in their experiment. In such a flow, the number of coherent structures distributed around the cylinder is typically very small, and the motion of the structures is likely to be strongly interrelated.

The findings of the present work are at variance with the hypothesis of Luxton et al. [1984] discussed earlier. However, the trends in the skewness and flatness profiles that led Luxton et al. to their hypothesis are supported by the present simulations (section 4.5). The changes in the profiles observed by Luxton et al. with increasing δ/a may actually be due to the decreasing values of a^+ in their experiments. Flow visualisations on transverse slices (section 6.1) suggest that the typical number of coherent flow structures distributed around the cylinder decreases

as a^+ decreases. The trends in the skewness and flatness profiles with decreasing a^+ are possibly a reflection of the decreasing complexity of the flow.

8.4 Mean Velocity Profiles

Turbulence quantities near a solid wall are generally found to scale with parameters derived from the mean wall-shear-stress τ_w, which is related to the wall-normal derivative of the mean velocity profile. In a Newtonian fluid with uniform dynamic viscosity μ, the value of τ_w is equal to $\mu\, d\overline{U}/dy$ evaluated at the wall. Two important parameters that are derived from τ_w are the friction velocity $u_\tau = \sqrt{\tau_w/\rho}$ and the skin friction coefficient $C_f = \tau_w/(\frac{1}{2}\rho V_\infty^2)$.

Mean velocity profiles in turbulent boundary layers on planar surfaces can be divided into three distinct regions. The innermost region, which extends from the wall to $y^+ = yu_\tau/\nu \approx 10$, is governed mainly by viscous effects. In this region, the velocity profile has the accepted form $\overline{U^+} = \overline{U}/u_\tau = y^+$. In the outermost region, which extends outwards from $y/\delta \lesssim 1$, the velocity profile has the form $(V_\infty - \overline{U})/u_\tau = f[y/\delta]$, where f is an empirically determined function. In the intermediate region, the inner and outer scaling laws overlap, and the resulting velocity profile has the accepted form $\overline{U^+} = 2.5\ln[y^+] + 5.1$, where the constants vary slightly depending on the Reynolds number. The forms of the mean velocity profile in the inner, outer and intermediate regions are respectively known as the law of the wall, the velocity-defect law and the logarithmic law.

In turbulent boundary layers on cylinders in axial flow, the form of the mean velocity profile is affected by transverse curvature of the wall. The law of the wall proposed by Rao [1967], $\overline{U^+} = a^+\ln[1 + y^+/a^+]$, appears to be a good fit to the present simulation results. The corresponding logarithmic law, $\overline{U^+} = 2.5\ln\big[a^+\ln[1+ y^+/a^+]\big] + 5.1$, is also a good fit to the simulation results, with the exception of flows having $a^+ \lesssim 20$. These flows do not appear to be fully turbulent outside the neighbourhood of the wall.

For a range of axisymmetric boundary layers, the values of $\overline{U^+}$ at $y = \delta$ plotted against the axisymmetric wall units of Rao [1967] evaluated at $y^+ = \delta^+$ (that is values of $\overline{U^+}[y = \delta]$ plotted against $a^+\ln[1+\delta/a]$) follow a nearly logarithmic profile. This observation leads to the empirical expression $V_\infty/u_\tau \approx 2.97\ln\big[Re_a\ln[1+\delta/a]\big] - 5.82$, which may be used to estimate wall-parameters such as a^+ and the skin friction coefficient C_f for given values of the outer-flow parameters Re_a and δ/a.

When the present simulation results are plotted in the planar velocity-defect form, $(V_\infty - \overline{U})/u_\tau$ versus y/δ, the profiles are strongly dependent on δ/a in the

outer part of the boundary layer. As δ/a increases, the slope of the cylinder profiles becomes less negative near $y/\delta = 1$, where the value of the velocity-defect is $0.01V_\infty/u_\tau$ by definition. The trend is consistent with the experimental observations and dimensional analysis of Willmarth et al. [1976]. Denli and Landweber [1979] formulate a velocity-defect law for thick, axisymmetric boundary layers, based on the idea that the outer flow is similar to an axisymmetric wake. The empirical constants in their formula are tuned to fit a limited number of experimental measurements, but the resulting velocity-defect law does not provide a reliable fit to the present data. It appears that further work may be necessary before a general scaling relation is devised for the mean velocity profile in the outer part of axisymmetric boundary layers.

8.5 Velocity-Scale for Axisymmetric Flow

The axial periodicity imposed on the cylindrical domain ensures that the present simulations of turbulence reach a statistically-steady state after a sufficient development time. The total shear-stress distribution at the statistically-steady state in axial flow can be expressed in analytical form. A corresponding expression can be derived for plane-channel flow. Comparison of the two expressions led Neves [1992] to propose a new velocity-scale for transversely curved boundary layers. In the present notation, the velocity-scale is

$$u_{\tau c}^2[y/h, b/a] = u_\tau^2 \left(\frac{1}{1 + (y/h)(b/a - 1)} \right) \left(\frac{b/a + 1 + (y/h)(b/a - 1)}{b/a + 1} \right), \qquad (8.1)$$

where h is the plane-channel half-width or the radial width $(b - a)$ of the cylindrical domain.

In a planar boundary layer, where $b/a = 1$, $u_{\tau c}$ is equivalent to the friction velocity u_τ. In an axisymmetric boundary layer, where $b/a > 1$, the value of $u_{\tau c}$ varies with distance y/h from the wall. The maximum value of $u_{\tau c}$ occurs at the wall, where $u_{\tau c} = u_\tau$, and the minimum value occurs at $y = h$, where $u_{\tau c} = u_\tau \sqrt{2/(b/a + 1)}$. Thus, when $b/a \approx 1$, there is little variation of $u_{\tau c}$ across the layer, and when b/a is large, the value of $u_{\tau c}$ in the outer part of the layer is significantly less than the friction velocity.

Near the cylinder wall, that is for $y \ll b + a$, the definition of the new velocity-scale reduces to $u_{\tau c} \approx u_\tau / \sqrt{1 + y^+/a^+}$. When a^+ is large, $u_{\tau c}$ is similar to the friction velocity at all wall-normal positions where the approximate definition is

valid. On the other hand, when a^+ is small, the near-wall values of $u_{\tau c}$ decrease substantially with increasing distance from the wall.

These properties of the velocity-scale $u_{\tau c}$ support the idea that, when a^+ is large, the effects of transverse curvature associated with non-zero values of δ/a ($b/a > 1$) are significant only in the outer boundary layer, and when a^+ is small, both the inner and outer portions of the boundary layer are affected by curvature. This idea underlies the categorisation of axisymmetric boundary layers into three flow regimes. They are described by Piquet and Patel [1999] and, with limiting values as suggested by Afzal and Narasimha [1985], are as follows:

(i) Small δ/a ($\lesssim 1$), large a^+ ($\gtrsim 250$). The flow is little affected by transverse curvature, and is effectively planar flow.

(ii) Large δ/a ($\gg 1$), small a^+ ($\lesssim 250$). Strong effects of transverse curvature are observed throughout the boundary layer, on both the inner and outer regions of the layer.

(iii) Large δ/a ($\gg 1$), large a^+ ($\gtrsim 250$). The effects of transverse curvature are mainly evident in the outer flow, which is similar to an axisymmetric wake.

Scaling relations based on the velocity-scale $u_{\tau c}$ successfully account for the effects of transverse boundary layer curvature on several different statistics computed from the results of the present simulations. In particular, for flows with similar values of δ^+ and different values of δ/a, the profiles of Reynolds shear-stress, in the form $\overline{u_r u_z}/u_{\tau c}^2$ versus y/h, collapse to a common curve throughout the boundary layer. Similarly, the RMS velocity profiles for flows with similar values of δ^+ collapse to a common curve when plotted in the form $u'/u_{\tau c}$ versus y/h, although the collapse is less than perfect near the wall for the radial and azimuthal components. The velocity-scale $u_{\tau c}$ is also useful for the derivation of a scaling relation for temporal wall-pressure spectra in the high-frequency range, as discussed in section 8.6.

The velocity-scale $u_{\tau c}$ is not directly applicable to experimentally measured data because it depends on the parameter b, which has no direct physical equivalent. A reasonable substitute for b may be $a + \delta$, where a is the cylinder radius and δ is the measured boundary layer thickness. Practical use of $u_{\tau c}$ is further complicated by the fact that the derivation of $u_{\tau c}$ assumes that the mean flow is not developing in the streamwise direction, which is tantamount to imposing a streamwise pressure-gradient. The definition of $u_{\tau c}$ may need to be modified in the absence of a pressure-gradient.

8.6 Temporal Spectra of Wall-Pressure

The wall-pressure in a turbulent boundary layer is generated by turbulent eddies that are distributed throughout the flow. The range of spatial scales and convection velocities of the turbulent eddies causes the temporal spectra of the wall-pressure fluctuations to scale in different ways in different frequency ranges. Farabee and Casarella [1991] and Bull [1996] identify four frequency ranges with different forms of spectral scaling in flow over flat plates.

The spectral scaling relations for cylinders in axial flow are considerably more complicated than those for flat plates, as a result of the effects of curvature on the flow. Empirical forms for the spectral scaling on cylinders have been determined from the present simulations. These are related to the flat-plate scaling relations in the mid-frequency and high-frequency ranges. The limited streamwise length of the computational domain and the low Reynolds numbers (δ^+) considered in the simulations do not allow useful comparisons of axisymmetric and flat-plate flow similarity to be made in the low-frequency and universal ranges.

The present simulation results for axisymmetric flow suggest that the temporal wall-pressure spectrum in the mid-frequency range has the form

$$\varphi_p u_\tau/(L_p\tau_w^2) = f_2\big[\omega L_p/u_\tau\big] \text{ for } 5 \leq \omega L_p/u_\tau \text{ and } \omega\nu/U_p^2 \leq 0.4, \tag{8.2}$$

where f_2 is a function and where

$$L_p = \delta/(1 + 0.4\delta/a). \tag{8.3}$$

The length-scale L_p is a replacement for δ in the mid-frequency scaling relation for flat-plate flow. The definition of L_p is based on the hypothesis that in flow at a given Reynolds number (δ^+), the outer portion of the flow contributes less to the wall-pressure as δ/a increases.

The contribution of the outer flow to the wall-pressure depends on both the intensity of the pressure-sources in the outer flow and the coupling between pressure-source intensity and wall-pressure. Profiles of RMS pressure-source intensity as functions of y^+ for the present simulations indicate that the pressure-source fluctuations in the outer flow become weaker as δ/a increases with the Reynolds number (δ^+) held steady. Analysis of the Green's function of the Poisson equation for pressure indicates that the coupling between pressure-source intensity and wall-pressure becomes weaker as δ/a increases. Thus, the wall-pressure contributed by the outer flow, and therefore the effective thickness of the boundary layer, is reduced by curva-

ture. The length-scale L_p is designed to be consistent with this trend. In the planar limit of $\delta/a = 0$, L_p is equal to δ, and as δ/a increases, the ratio L_p/δ decreases. For $\delta/a \geq 2.5$, L_p is biased towards the cylinder radius ($L_p \leq \delta/2$).

In the high-frequency range, the present axial-flow simulations suggest a spectral scaling relation of the form

$$\varphi_p/(\nu\rho^2 U_p^2) = f_4\big[\omega\nu/U_p^2\big] \text{ for } \omega\nu/U_p^2 \geq 0.4, \tag{8.4}$$

where f_4 is a function and where

$$U_p = u_\tau/\sqrt{1 + 20/a^+}. \tag{8.5}$$

The velocity-scale U_p and the corresponding stress-scale ρU_p^2 replace u_τ and τ_w in the high-frequency scaling relation for flat-plate flow. U_p is an approximation to $u_{\tau c}$ (equation 8.1) at $y^+ = 20$, which is the approximate location of the maximum fluctuation intensity of the pressure-source field. Pressure-sources near this position are presumed to make the dominant contribution to the wall-pressure in the high-frequency range of the spectrum. For planar flow ($a^+ = \infty$), U_p is equal to u_τ, and as a^+ decreases, the ratio U_p/u_τ decreases. The value of U_p is greater than 90% of u_τ for all flows except those with $a^+ < 85$.

The scaling relations presented above are consistent with available experimental data for cylinders in axial flow. The cylinder relations asymptotically approach the flat-plate relations as the radius of the cylinder increases.

The RMS wall-pressure p' may be obtained from the temporal spectrum by integration. The values of p' in the present simulations, when normalised by the wall-shear-stress τ_w, are strongly dependent on the length-scale L_p. The empirical formula $p'/\tau_w = 1.61\log[L_p^+] - 2.04$ is a good fit to the available cylinder data and also to the plane-channel results of Moser et al. [1999] and the flat-plate measurements of Farabee and Casarella [1991]. The present formula differs from that obtained by Farabee and Casarella, but it is not clear which of the two formulae is the more reliable (over the range $100 \lesssim L_p^+ \lesssim 3000$) due to the considerable scatter in the available data. Some of the experimental results may be subject to the effects of inadequate sensor resolution or local discontinuities in the wall surface caused by pin-hole connections to the sensors. The reliability of the present simulation results is enhanced by the absence of pin-holes and by spatial resolution that is better than most experiments ($\Delta z^+ \approx 12$, $a^+\Delta\theta \lesssim 4$), particularly in the azimuthal direction. However, the present simulations and some experiments are subject to a streamwise pressure-gradient, the effect of which is not well understood. To isolate or eliminate

the effects of these systematic variations between different investigations, additional measurements or calculations of wall-pressure may be necessary.

8.7 Turbulent Near-Axial Flow

The vorticity-based simulation procedure used for the present investigation is designed to accommodate a free-stream that is inclined at an angle β to the cylinder axis. Axial flow is simply the special case $\beta = 0$. The lack of axisymmetry in yawed flow implies that the outer radial boundary of the cylindrical computational domain may cause truncation and distortion of the flow on the leeward side of the cylinder in simulations of yawed flow produced by the present procedure. To avoid this problem, data are collected from the present simulations of turbulent yawed flow after a suitable development time but before significant vorticity accumulates near the outer domain boundary. The simulations are stopped well before the statistically-steady state is reached.

The lack of both statistical steadiness and axisymmetry complicates the averaging of flow statistics. The method adopted here is to average over small temporal and azimuthal intervals, in addition to averaging over the axial length of the domain. The calculation of flow statistics may be improved, however, by use of ensemble averages instead of the azimuthal and temporal averages used for the present work. Data for the ensemble averages may be taken from corresponding time-steps of several simulations of the same flow case, with initial conditions for each simulation taken from different time-steps of an axial-flow simulation.

Calculated flow statistics are dependent on the initial conditions used for simulation until a sufficient development time has elapsed. Beyond this time, the flow statistics are characterised by values of the yaw angle β, the Reynolds number Re_a and the displacement thickness δ^*/a. It is not possible to relate the simulation results to an absolute streamwise position, except by comparison with experimental results, due to the imposed axial periodicity of the computational domain.

Simulations of turbulent boundary layers have been performed for several yaw angles ($\beta = 0.25°, 0.5°$), Reynolds numbers ($Re_a = 311, 674$) and displacement thicknesses ($\delta^*/a < 1.3$). No previous flow simulations of near-axial flow appear to have been reported in the literature.

Contours of mean velocity indicate that the asymmetry of the flow is considerably greater than might be expected intuitively for the very small yaw angles considered, although in this respect, the present results are consistent with the experimental results of Willmarth et al. [1977]. As the yaw angle increases, contours move

closer to the cylinder on the windward side and further away on the leeward side. Mean velocity profiles in wall units, based on the azimuthally averaged friction velocity $\overline{u_\tau}$, are higher on the windward side and lower on the leeward side of the cylinder. In the logarithmic region, the yawed-flow profiles are shifted upwards or downwards depending on azimuthal position, but the slope of the profiles is nearly independent of azimuthal position and is very similar to that of the logarithmic region in axisymmetric flow with the same value of Re_a. The effects of free-stream yaw on the logarithmic region are consistent with those found experimentally by Bücker and Lueptow [1998].

Profiles of turbulence statistics, including Reynolds shear-stress, RMS velocity, RMS vorticity and RMS pressure, when plotted in wall units based on $\overline{u_\tau}$, are lower on the windward side and higher on the leeward side of the cylinder, which is the opposite of the trend noted for the mean velocity profiles. The difference between the RMS wall-pressures on the leeward and windward sides of the cylinder is of the opposite sign from that found experimentally by Willmarth et al. [1977] and Berera [2004]. The discrepancy may be connected with the low value of Re_a (674) used for the simulations compared with the Reynolds numbers used for the experiments (3300 and larger). In the present simulations, the turbulence appears to be intermittent on the windward side of the cylinder, whereas the higher Reynolds numbers considered in the experiments almost certainly correspond to fully turbulent flow.

Despite this discrepancy, the plausible results produced by the present simulation procedure suggest that the numerical scheme is suitable for use in future investigations of turbulent boundary layers on cylinders in near-axial flow.

8.8 Vortex-Shedding in Near-Axial Flow

The experiments of Bull and Dekkers [1993a] show that a form of vortex-shedding occurs when the yaw angle β exceeds a threshold that depends on the Reynolds number Re_a. To investigate this phenomenon further, a yawed-flow simulation has been performed with the parameters $\beta = 3^\circ$ and $Re_a = 311$. The simulation has been advanced in time sufficiently to allow the initial condition, an axisymmetric, turbulent boundary layer, to develop into vortex-shedding flow. The vortices appear to be shed at an angle to the cylinder, with one end remaining attached to and travelling along the cylinder.

Graphs of the axial component of velocity as functions of either time or axial position feature continuous oscillations with a uniform temporal or spatial period. The velocity oscillations have the character of a wave travelling in the axial direction

at the same speed as the axial component of the free-stream, regardless of the local velocity of the flow.

Vortex lines appear to form closed loops around the cylinder and are stretched towards the wake. The azimuthal orientation of the vortex loops varies in a wave-like fashion along the length of the cylinder. The three-dimensional structure of the vorticity field suggests that the classification "vortex-shedding" is not strictly accurate, because individual vortex structures are observed only in two-dimensional slices of the flow. However, the term vortex-shedding is used here for consistency with the existing literature on the subject.

The time-varying wall-pressure on opposite sides of the cylinder may excite transverse vibration of a flexible cylinder. However, the present simulation indicates that so-called vortex-shedding is possible in the absence of cylinder vibration or specific end-effects, none of which are included in the computational model.

Early investigations of yawed flow over cylinders [see, for example, Chiu and Lienhard, 1967] invoke the so-called "independence principle", which is the notion that the components of free-stream velocity normal to and parallel with the cylinder may be regarded as independent. The experimental results of van Atta [1968], amongst others, indicate that the independence principle only holds for a limited range of yaw angles in the neighbourhood of cross-flow ($\beta \approx 90°$). In the present yawed-flow simulation, the Reynolds number normal to the cylinder, $aV_X/\nu \approx 16$, is so low that steady laminar flow would be expected for a cylinder in cross-flow. The fact that vortex-shedding occurs instead is further evidence that the independence principle is not valid at small yaw angles.

8.9 Future Work

Flow simulations performed as part of the present investigation have generated a large amount of detailed, quantitative data describing the turbulent boundary layer on a cylinder in axial flow. The range of flows investigated has allowed the effects of transverse curvature to be identified at Reynolds numbers (δ^+) that are relatively small by experimental standards. To establish the significance, or otherwise, of some of these curvature effects at larger Reynolds numbers, there may be merit in performing additional simulations once the inevitable improvement in computer technology makes such an exercise practical.

A small number of yawed-flow cases have been simulated in the present investigation, and the results agree qualitatively with relevant experimental data. There is considerable scope for a future investigation to extend the simulations to a wider

range of yaw angles, Reynolds numbers and boundary layer thicknesses. Such an investigation would help to clarify and extend the limited amount of experimental data that are currently available.

The results reported here for axisymmetric boundary layers correspond to the statistically-steady state, which is associated with a streamwise pressure-gradient. However, the bulk of the experiments, and many of the applications, concerning axisymmetric boundary layers do not involve streamwise pressure-gradients. Therefore, a worthwhile improvement to the axial-flow simulation procedure would be the elimination of the streamwise pressure-gradient. One possible approach is similar to that used for the yawed-flow simulations, where data are collected before the statistically-steady state is reached.

Finally, it is important to note that direct numerical simulation of turbulent flow is very demanding of computational resources. Simulation of flow at Reynolds numbers comparable with some engineering applications may only be possible using advanced, model-based methods such as Large Eddy Simulation. Before such methods can be used with confidence, the underlying models may need to be validated in the context of boundary layers with transverse curvature. Some steps in this direction have recently been taken by other researchers [see, for example, Tutty et al., 2004].